

RESEARCH ARTICLE

10.1029/2019JB019333

Key Points:

- We used intercomponent cross-correlations methods to analyze seismovolcanic signals at Piton de la Fournaise volcano
- The application of our methods allowed detection and classification of the three eruptive tremors that occurred in 2010
- We have located tremor and VT sources and highlighted a pre-eruptive seismic sources migration from the sea level to the eruptive site

Supporting Information:

- Supporting Information S1

Correspondence to:

C. Journeau,
 cyril.journeau@univ-grenoble-alpes.fr

Citation:





Journeau, C., Shapiro, N. M., Seydoux, L., Soubestre, J., Ferrazzini, V., & Peltier, A. (2020). Detection, classification, and location of seismovolcanic signals with multicomponent seismic data: Example from the Piton de la Fournaise volcano (La Réunion, France). *Journal of Geophysical Research: Solid Earth*, 125, e2019JB019333. <https://doi.org/10.1029/2019JB019333>

Received 31 DEC 2019

Accepted 22 JUN 2020

Accepted article online 27 JUN 2020

Detection, Classification, and Location of Seismovolcanic Signals with Multicomponent Seismic Data: Example from the Piton de La Fournaise Volcano (La Réunion, France)

C. Journeau^{1,2} , N. M. Shapiro^{1,3} , L. Seydoux¹ , J. Soubestre⁴ , V. Ferrazzini^{5,6} , and A. Peltier^{5,6} 

¹Institut des Sciences de la Terre, Université Grenoble Alpes, CNRS (UMR5275), Grenoble, France, ²Département de Géosciences, Ecole Normale Supérieure, PSL Res. Univ., Paris, France, ³Schmidt Institute of Physics of the Earth, Russian Academy of Sciences, Moscow, Russia, ⁴Instituto Volcanológico de Canarias (INVOLCAN), Granadilla de Abona, Tenerife, Canary Islands, Spain, ⁵Université de Paris, Institut de Physique du Globe de Paris, CNRS, Paris, France, ⁶Observatoire Volcanologique du Piton de la Fournaise, Institut de Physique du Globe de Paris, Université de Paris, CNRS (UMR 7154), La Réunion, Paris, France

Abstract We apply three different methods based on the analysis of the multicomponent seismic data to detect seismovolcanic tremors and other seismovolcanic signals, to propose an approach to classify them, and to locate their sources. We use continuous seismograms recorded during 1 year by 21 stations at the Piton de la Fournaise volcano (La Réunion, France). The first method allows the detection of seismovolcanic signals based on stability in time of the intercomponent cross-correlation function. Two other methods based on the simultaneous analysis of the whole network can be used to detect seismovolcanic signals and to locate their sources. In the first network-based method, the seismic wavefield is analyzed by calculating the width of the network covariance matrix eigenvalue distribution. The second network-based method consists in performing the 3-D backprojection of the interstation cross correlations in order to calculate the network response function. Simultaneous analysis of the parameters measured by the three different methods can be used to classify different types of seismovolcanic tremors. Our results demonstrate that all three methods efficiently detect seismovolcanic tremors accompanying the 2010 eruptions and the preceding pre-eruptive seismic swarms. Furthermore, Methods 2 and 3 based on simultaneous analysis of the whole network detect a large number of volcanic earthquakes. Our location results show that each seismovolcanic tremor is located in a distinct region of the volcano, close to the eruptive site at a shallow depth, and the preceding seismic crisis is located deeper at about the sea level under the summit crater.

1. Introduction

Volcanic activity is generally accompanied by a large spectrum of seismic signals from pre-eruptive seismic swarms to seismovolcanic co-eruptive tremors (e.g., McNutt & Roman, 2015). The generation of seismic waves in volcanoes might be related either to the release of mechanical stresses within the volcanic edifices and underlying crust (e.g., Roman & Cashman, 2006) or to the movement of magma and related hydrothermal fluids and to their complex interactions with solid rock (e.g., Chouet, 1996). The interpretation of these signals and the quantification of their source mechanisms allow us to better understand the oscillatory behavior of volcanic systems and provide information about the underlying physical processes. Thus, seismovolcanic data play a fundamental role in observing and understanding ongoing processes within active volcanic systems and are critical for monitoring volcanoes and anticipating their eruptive behavior.

Collection of the seismological data on volcanoes is rapidly advancing because of the modern technological developments. More and more volcanoes are equipped with networks composed of several very sensitive and broadband seismographs recording continuous data and transmitting them more broadly and in real time to volcano observatories. Archived continuous data sets and real-time data streams from several volcanoes are available through main international data centers and data collecting systems such as IRIS (<https://ds.iris.edu/ds/nodes/dmc/>) and ORFEUS/EIDA (<http://www.orfeus-eu.org/data/eida/>). This rapid

increase in data quality, quantity, and availability opens new opportunities for seismovolcanic monitoring.

At the same time, a full exploration of information contained in seismovolcanic data is a very challenging problem. Many of the methods used in today's volcano seismology are inherited from the past and were initially developed for a manual or weakly automated analysis of very light data streams. Single-station and/or event counting approaches remain dominantly used in the seismic volcano monitoring. These approaches have a significant advantage of being simple and robust, making their implementation possible in the majority of volcano observatories suffering from the lack of resources and infrastructure. Nevertheless, even with massive implementation of these simple methods, the information contained in the seismovolcanic data remains very poorly used.

A full and coherent exploration of the information provided by modern seismovolcanic monitoring facilities requires a more systematic usage of advanced network-based methods. Most advanced volcanic observatories are developing computing infrastructure that allows "in situ" implementation of such methods. In a case of less well equipped observatories, the data streams can be transmitted to larger regional or national (and eventually international) data analysis centers where advanced algorithms requiring significant computing power can be applied. The results of such advanced seismological analysis can be then retransmitted back to the observatories to be incorporated with other collected data and information for evaluation of the state of the volcanoes.

Network-based seismological methods are recognized as having a large potential for improving volcano monitoring because of their capacity to detect signals different from "regular" earthquakes and to locate/characterize their sources. The main idea of the network-based analysis is, instead of trying to detect signals at individual records, characterizing the level of spatial coherence of a wavefield as it is recorded by the ensemble of instruments. As a result, they do not generate discrete catalogs of events but continuous functions representing the properties of the recorded wavefields and, in favorable conditions, can be "back-propagated" to characterize the emitting sources.

Network-based methods are particularly well adapted for analysis of seismovolcanic tremors (e.g., McNutt & Nishimura, 2008) that are part of the long-period (LP) seismicity (Chouet, 1996). These ground vibrations with a sustained amplitude lasting from minutes to months, characterized by a low-frequency content (0.5–5 Hz), accompany eruptions and are often synonymous with the arrival of magma at the subsurface and the first signs of degassing. Therefore, they are a key element in volcano monitoring, and a thorough study of these signals could allow us to bring new information about volcanic system and to develop new methods of eruption forecasting. They can be caused by several volcanic processes including magma-hydrothermal interactions and magmatic degassing (e.g., Chouet & Matoza, 2013), but their physical origin is poorly understood, and the study of their source is part of the current challenges of the modern volcanic seismology.

The network-based methods can be also useful in characterizing volcanic earthquakes. In some cases, their time resolution can be enhanced to resolve individual events. Alternatively, smoothed network-response functions can be considered as proxies to the properties of the swarms composed of many earthquakes and to infer their approximate source locations.

Network signal analysis is a very large family of methods (Rost & Thomas, 2002), and several of them have been used in volcano seismology. Different methods are based on their own sets of assumptions, resulting in different network-response functions with different detection capabilities and resolutions (in space, time, and frequency domains). Simultaneous application of different network-based methods can provide us with complementary information necessary to detect and to identify different types of volcanic activity. Testing this multimethod approach was the main motivation for our present work. We focused on three different methods and looked to applied them to a data set from a volcano with well-known activity. For this reason, we selected Piton de la Fournaise (PdF) volcano (La Reunion island, France). This volcano is one of the most active in the world and is systematically observed by the Observatoire Volcanologique du Piton de la Fournaise (OVPF) with different monitoring techniques and, in particular, with a modern network of broadband seismographs.

The first of the tested methods is new (has been developed in this study) and explores the stability of inter-component cross correlations to detect tremors. In a simplest case, it can be used in a single-station mode.

The two other methods are existing interstation cross-correlation, network-based approaches described by Seydoux, Shapiro, De Rosny, et al. (2016) and by Droznin et al. (2015). The latter has been modified here to be computed on a 3-D grid. We compare these three methods in terms of volcano-seismic signal detection. We also show how the simultaneous analysis of the parameters measured by the three different methods can be used to separate the different types of detected signals, which suggests a potential application to classify them. Moreover, we will also present locations of sources detected by the network-based methods. The location method is from Soubestre et al. (2019), but here the temporal resolution is enhanced to study the pre-eruptive seismic crises. Thus, another motivation of our study is to show how these methods can be applied to follow the pre-eruptive seismic processes and seismovolcanic tremor activity through time and space.

We analyze the data recorded by the PdF seismic network during 2010 when three eruptions occurred (see Figure 1 for the positions of eruptive fissures and associated lava flows):

- *the January eruption* that lasted 11 days from 2–12 January 2010, with the eruptive fissure located on the west part of the summit cone, inside the Dolomieu crater;
- *the October eruption* that lasted 17 days from 14–31 October 2010, with the eruptive site located in the south flank of the volcano; and
- *the December eruption* that lasted about 15 hr between 9 and 10 December 2010, with the eruptive site located in the northwestern part of the caldera.

These three eruptions were preceded by pre-eruptive seismic crises and accompanied by seismovolcanic tremors starting at the onset of the eruption. Examples of seismograms and of real-time seismic amplitude measurements (RSAM) (Endo & Murray, 1991) during the January and October eruptions are shown in Figure S1 in the supporting information.

PdF volcano and its seismic network are introduced in section 2. Then, a rapid description of its seismovolcanic tremors is made in section 3. The methods applied in this study are described in section 4, with the obtained results presented in section 5 and discussed in section 6.

2. PdF Volcano and the Seismic Monitoring System

La Réunion is a volcanic island located in the southwest of the Indian ocean in the Marscarene Basin (Figure 1). Based on dating and geodynamic reconstruction, its volcanism is thought to have a hot spot origin and to have been generated by the same mantle plume that produced the Deccan Trapp about 65 Ma (Courtillot et al., 1986). The head of this mantle plume would have passed beneath La Réunion about 5 Ma and would be now located 300 km southwest of the island (Bonneville, 1990). Tsekhmistrenko et al. (2018) present a high-resolution body-wave tomography of the whole mantle column beneath the western Indian Ocean providing a more complex view of the plume beneath La Réunion. Their model reveals that the upwelling shows considerable tilt in the lower mantle instead of being near-vertical and splits into branches near the surface.

The PdF volcano is an intraplate shield basaltic volcano of Hawaiian type located in the southeast part of the island. It is 2,631 m high and active since about 530 ka. Throughout its existence, this volcano has been marked by the formation of successive concentric calderas, the latest being the Enclos Fouqué, formed about 4,500 years ago (Bachelery, 1981), in which there is a summit cone 400 m high and 3 km wide at its base with two craters: the Bory crater and the Dolomieu crater, the latter being the most active one.

The PdF is considered as one of the most active volcanoes in the world, with approximately one eruption occurring every 9 months in average. Thus, its very frequent eruptions weakly dangerous for the population (97% of the recent eruptions occurred within the uninhabited caldera) make it an ideal natural laboratory to study active volcanic processes.

Geodetic and seismic data suggest the presence of a shallow magma reservoir around $2,500 \pm 1,000$ m below the PdF summit craters (Staudacher et al., 2016). However, the exact geometry of storage zones and their possible interconnections are still debated. While Lénat and Bachelery (1990) suggested the presence of small magma pockets scattered between the summit and the sea level, Peltier et al. (2008) inferred from geodetic data a single magma reservoir located above the sea level, regularly recharged by a deeper source.

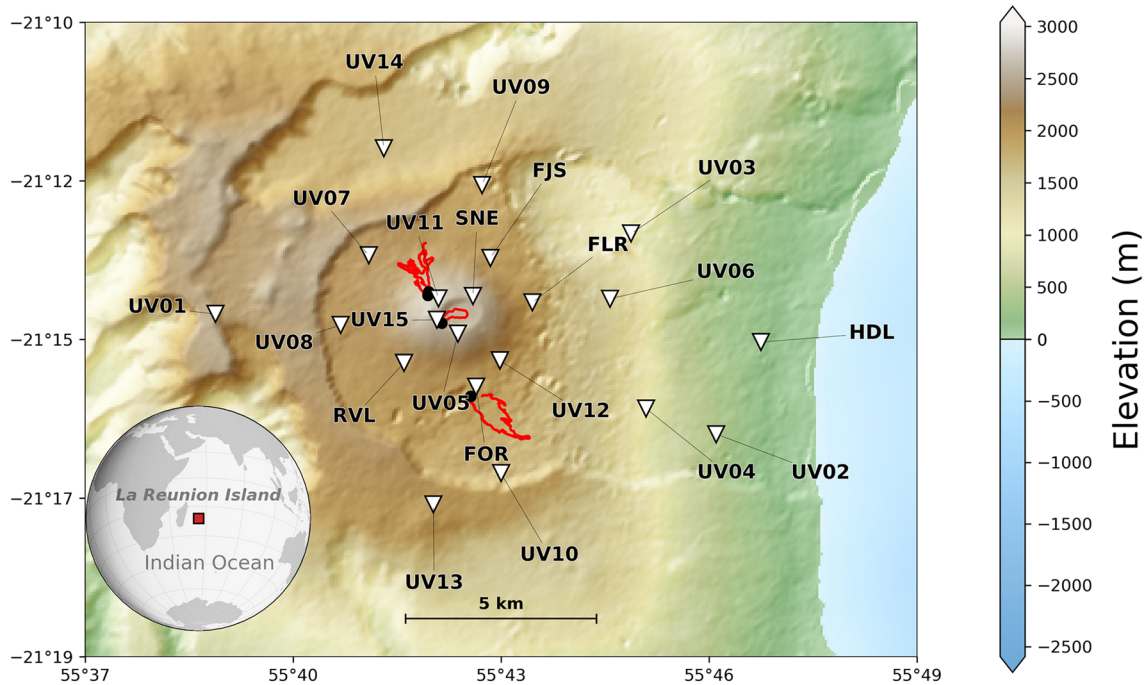


Figure 1. Color-shaded relief map of the Piton de la Fournaise volcano, located on the southeast part of La Réunion island. The bottom left inset shows the location of La Réunion island in the Indian Ocean. Seismic stations used in this study are represented with white inverted triangles. Black dots stand for the position of the eruptive fissures corresponding to the January, October, and December 2010 eruptions, located at the west part of the summit cone, south flank, and northwest flank, respectively. Red lines stand for the lava flows associated with these eruptions.

Since the installation of the volcano observatory of PdF (OVPF) in 1979, the seismic network has evolved from a small number of short-period stations recording on a triggered basis to a modern network combining broadband and short-period sensors and recording continuously (Battaglia et al., 2016). In 1999, there were 19 short-period stations in the network, mostly installed near the summit and around the volcano. In May 1999, continuous recording appeared with storage on CD-ROMs, and the network was completed after the 2007 Dolomieu crater collapse, including up to six broadband three-component stations by the middle of 2009. Since October 2009, 15 broadband stations located on the volcano were installed as part of the Understanding Volcano project (UnderVolc) (Brenquier, 2014; Brenquier et al., 2012), in addition to the existing seismic network. Figure 1 shows the 21 broadband three-component stations present in 2010 that we use in this study.

3. Seismovolcanic Tremor of PdF Volcano

The PdF seismovolcanic tremors are generally coeruptive, starting when the eruption begins and disappearing at the end. It is characterized by a relatively broad spectrum around 0.5–10 Hz (Battaglia & Aki, 2003).

The signals generated by seismovolcanic tremors are generally emergent, without any clear onset. This implies a lack of seismic phase identification and prevents the use of traditional strategies for seismovolcanic tremor source location. Therefore, this is necessary to develop new methods better suited for its analysis. Battaglia and Aki (2003) proposed a method based on seismic amplitudes for locating events. They showed that once corrected for station sites effects using coda site amplification factors, the spatial distribution of amplitudes shows smooth and simple contours for events including LP events and seismovolcanic tremor. Following this approach, Battaglia et al. (2005) located sources of several coeruptive seismovolcanic tremors at the PdF and found that they better correlated with the position of the eruptive vents for the 5–10 Hz band, suggesting a generation directly located at the eruptive site. While for frequency above 1.5 Hz, the seismovolcanic tremor sources are generally found at shallow depth, they suggest that lower frequencies could be related to deeper processes rather than directly by the eruption observed at the surface. Taisne et al. (2011) used a similar method to study the PdF pre-eruptive seismic crises.

4. Methods

Most volcano observatories monitor seismovolcanic tremor in real-time based on measuring their amplitudes at a single reference station located near the volcano (e.g., Endo & Murray, 1991). The idea of this approach is that the position of the seismovolcanic tremor source remains more or less stable in time and that the amplitude of the seismic signal can be considered as a proxy of the intensity of the seismovolcanic tremor generating processes. This single-station/component approach can be developed further with the use of the spectral shape of the signal (instead of its averaged amplitude) leading to a better discrimination of different phases of seismovolcanic tremor (Unglert & Jellinek, 2015; Unglert et al., 2016). One of the main difficulties of single-component approaches is that they cannot be used to get information about the spatial location and extent of the source. In particular, this might result in difficulties with distinguishing seismovolcanic tremors from other types of processes leading to increased seismic amplitudes such as, for example, meteorological and anthropogenic noises.

In this paper, we systematically use and compare methods based on correlations of signals to perform detection and location of seismovolcanic signals. We first briefly describe the data preprocessing used in all analyses considered in this paper. Then, we introduce a single-station method aimed at detecting long-acting sources based on stability of intercomponent cross correlations. In a next step, we consider methods based on simultaneous analysis of the whole network of receivers. Our approach is different from the antenna-type detection of seismovolcanic tremors based on small-aperture arrays and plane-wave approximation for measuring slowness and azimuth of incoming wave (e.g., Goldstein & Chouet, 1994; Haney, 2014; Métaxian et al., 2002). We rather consider a geometry where the source of seismic radiation is located within the network. It implies that the moveouts are not described with plane waves but with a wave propagation from a point source (cylindrical wave in a case of surface waves and ray-predicted times for body waves). In this case, it has a strong imprint on interstation cross correlations (e.g., Ballmer et al., 2013; Droznin et al., 2015; Shapiro et al., 2006). In volcanic environments, these cross correlations can be used to detect seismovolcanic signals and to locate their source. Here we apply two network-based methods. First, we use the representation of ensemble of interstation cross correlations in terms of network covariance matrix suggested by Seydoux, Shapiro, De Rosny, Brenguier, et al. (2016); Seydoux, Shapiro, de Rosny, and Landes (2016) and Seydoux et al. (2017) and used by Soubestre et al. (2018, 2019) to study seismovolcanic tremors. Second, we adapt on a 3-D grid the approach of Droznin et al. (2015) that backproject the cross-correlation envelopes in time using a 1-D S wave velocity model to detect seismovolcanic signals, and we follow the approach described in Soubestre et al. (2019) to locate their sources.

We focus on the information contained in the time variations of the signal phase differences between stations. We also consider the instrument response of the seismic stations to be stable over time and, therefore, do not consider instrument correction. We then further apply the preprocessing usually performed in ambient-noise interferometry (e.g., Bensen et al., 2007; Shapiro & Campillo, 2004; Shapiro et al., 2005).

The data are stored in 24-hr-long time series in SAC downsampled from 100 to 20 samples per second. We apply demeaning, linear detrending, and bandpass filtering between 1 and 10 Hz. Then, a spectral whitening is applied followed by a temporal normalization according to Bensen et al. (2007).

4.1. Single-Station Intercomponent Cross Correlations

We present here a new method to detect some seismovolcanic signals including seismovolcanic tremors based on the stability of the intercomponent cross correlations at a single station. Let us consider a wavefield generated by a seismovolcanic tremor source that remains at the same location and with a constant source mechanism. As argued by Droznin et al. (2015) and Soubestre et al. (2018), the cross correlation of such a wavefield between two receivers will remain stable in time and can be used as a “fingerprint” of this particular source. This principle also holds for a cross correlation between two components of the same receiver, and we use this property to design a simple single-station seismovolcanic tremor detector. We start with computing intercomponent cross correlations $CC_{i,j}(i,j=E,N,Z)$ in moving windows of length Δt and shifted by $\Delta t/2$. We then compute correlation coefficients between cross-correlation waveforms from consecutive time windows and take the mean value of six consecutive computations. The obtained functions $cc_{i,j}^6$ provide us with estimation of the stability of the cross-correlation waveforms that, in turn, is related to existence of stable seismovolcanic tremor source. In our case, we use moving windows of length $\Delta t=200$ s to compute

intercomponent cross correlations, and therefore, the $cc_{i,j}^6$ functions correspond to a short-term estimation of the cross-correlation waveform stability over 700 s. The $cc_{i,j}^6$ function is represented in section 5.1. This method allows us to detect seismovolcanic tremor activity by using only one component pair of a single seismic station. In order to improve the seismovolcanic tremor detection results, we can first average the three $cc_{i,j}^6$ functions obtained from the three component pairs of one single station and then average the previous functions on several stations.

4.2. Interstation Single-Component Cross Correlations: Covariance Matrix Spectral Width

We use the method proposed by Seydoux, Shapiro, De Rosny, et al. (2016) where an ensemble of interstation cross correlations is computed in the frequency domain (also called network covariance matrix). This matrix is decomposed on the basis of its eigenvectors associated with real positive eigenvalues. The main idea behind this method is to consider that the rank of the covariance matrix (number of nonzero eigenvalues) is related to the number of independent signals composing the wavefield and then of independent seismic sources. A single source would generate a rank 1 covariance matrix, and this rank would increase with the number of independent sources. However, because of the presence of seismic noise (generated by ocean microseismicity, wind, etc.) and instrumental electronic noise in the data, it is complicated to estimate the effective rank of the covariance matrix, and the number of independent sources cannot be directly inferred. In addition, as the covariance matrix is estimated from a finite number of windows, this may reduce the ability to capture the independent seismic signals. Nevertheless, the width of the covariance matrix eigenvalues spectrum ($\sigma(f)$ called spectral width) can be used as a proxy for the number of independent seismic sources composing the wavefield (Seydoux, Shapiro, De Rosny, et al. 2016). Thus, this spectral width is high when it corresponds to ambient seismic noise produced by distributed sources, while it is low when it corresponds to a spatially coherent signal produced by a single localized source, such as seismovolcanic tremor and volcano-tectonic earthquakes (VTs).

Following Seydoux, Shapiro, De Rosny, et al. (2016), we start by cutting the daily traces into a number of overlapping time windows that we call averaging windows. Then, each averaging window is cut into M overlapping subwindows of length δt such that $\Delta t = Mr\delta t$, where Δt is the length of the averaging time window and r the overlapping ratio that is 0.5 on our case. We apply a taper on the data prior to calculating the Fourier transform on the subwindow to avoid sharp windows; that is why the signal segments are overlapped with a factor of 50% in order not to lose any information located in consecutive windows. We then collect the array data vector from the N seismic stations $\mathbf{u}(f)$ as $\mathbf{u}(f) = [u_1(f), u_2(f), \dots, u_N(f)]^T$ and compute the outer product $\mathbf{u}(f)\mathbf{u}^\dagger(f)$ within each subwindow, where \dagger stands for the Hermitian transpose. Then the covariance matrix $\mathbf{C}(f)$ is estimated on any averaging window from M consecutive subwindows:

$$\mathbf{C}(f) = \langle \mathbf{u}(f)\mathbf{u}^\dagger(f) \rangle_{\Delta t} = \frac{1}{M} \sum_{m=1}^M \mathbf{u}_m(f)\mathbf{u}_m^\dagger(f), \quad (1)$$

with $\mathbf{u}_m(f)$ the data Fourier spectra vector in the subwindow m . Note that the inverse Fourier transform of Equation 1 is the interstation single-component cross correlation estimated over the M subwindows.

This calculation can be extended on consecutive averaging window over the whole year 2010 with $M=50$ and $\delta t=40$ s. We note that δt must be long enough for the seismovolcanic tremor seismic wave to have time to propagate through the entire network. We thus obtain 1,000-s-long windows that overlap with a 50% factor. The obtained covariance matrix is Hermitian and positive semidefinite, so it can be decomposed on the basis of its complex eigenvectors \mathbf{v}_n associated with real positive eigenvalues λ_n :

$$\mathbf{C}(f) = \sum_{n=1}^N \lambda_n(f) \mathbf{v}_n(f) \mathbf{v}_n^\dagger(f). \quad (2)$$

Then eigenvalues are arranged in decreasing order and the covariance matrix spectral width is computed as a function of frequency as

$$\sigma(f) = \frac{\sum_{i=1}^N (i-1) \lambda_i(f)}{\sum_{i=1}^N \lambda_i(f)}. \quad (3)$$

4.3. Interstation Single-Component Cross Correlations: Network Response and Source Location

4.3.1. Detection of Seismovolcanic Signals From Full-Rank Interstation Cross-Correlation Matrix

We follow the approach of Droznin et al. (2015), who developed a 2-D source-scanning algorithm based on the stacks of interstation cross-correlation envelopes, in order to detect seismovolcanic tremors and to locate their sources. This method is based on an assumption that seismovolcanic tremor source is relatively shallow and that seismic energy propagates toward the stations along the surface. The differential travel times of signals emerging in interstation cross correlations are then interpreted in terms of surface wave (2-D) propagation in order to find the geographical location of the seismovolcanic tremor source. Here we apply this method in a 3-D grid in order to locate also deeper seismovolcanic sources such as VTs. The location is done by performing a 3-D grid search with tested sources spaced 200 m apart. We first compute the interstation cross correlations (we only use the vertical component seismograms) between all pairs of available stations. We therefore end up with 210 pairs of cross correlations when data from the 21 stations are available. The next step consists in computing the smoothed envelopes of the cross-correlation waveforms. This is done by computing the absolute value of the analytic signal derived from the Hilbert transform and by performing a convolution with a 3-s-long Gaussian window. Then, for every tested source position in our 3-D grid, we compute travel times for all stations using a 1-D *S* wave velocity model of the PdF volcano from Mordret et al. (2015) (shown in Figure S2) by considering that seismovolcanic tremors and their cross correlations are dominated by *S* waves (Soubestre et al., 2019). We note that the weak *S* wave velocities observed in the near-surface layers constituted of poorly consolidated volcanic materials (Figure S2) are consistent with the horizontal wave propagation velocity that we can estimate as seen in Figure S3 by performing a linear regression between the maxima of the smoothed cross-correlation envelopes. Figure S3 represents the smoothed cross correlations calculated between the UV05 station (the closest available station to the January eruptive center) and all the others available stations for 3 January 2010. We chose the UV05 station because we assume that the source of the seismovolcanic tremor is located close to the January eruptive center and its position is stable. The red line is the result of the linear regression whose slope corresponds to a horizontal wave propagation velocity of 700 m/s. We also observe similar velocities for other days with seismovolcanic tremor activity.

Then, for every point $\mathbf{r} = x\mathbf{e}_x + y\mathbf{e}_y + z\mathbf{e}_z$, each cross-correlation envelope $S^{i,j}$ is shifted by the time difference needed for the wave to travel from the tested source to the two stations i and j , and we finally compute the network response $R(\mathbf{r})$ by stacking at zero lag time the value of the shifted envelopes for all station pairs as

$$R(\mathbf{r}) = \sum_{i=1}^N \sum_{j=i+1}^N S^{i,j}[t^i(\mathbf{r}) - t^j(\mathbf{r})], \quad (4)$$

with N the number of stations and $t^i(\mathbf{r})$ the travel time between the tested source and the station i . This network response (called likelihood afterwards) characterizes the likelihood of location of a seismic source in a particular position. Finally, we calculate the normalized maximum network response called NRF afterwards for network response function

$$NRF(n) = 100 \times \frac{R^{\max}(n) - R^{\min}(n)}{R^{\text{ref}}} \quad (5)$$

for every day of 2010, where n is the day number and R^{ref} a normalization coefficient chosen as an average of $R^{\max} - R^{\min}$ over the October 2010 eruption, the longest period of seismovolcanic tremor activity during the year. The function is defined in such a way that it maximizes when most of its values are concentrated in the vicinity of the main maximum, that is, in a case of a strong localized source. The NRF is then used as a proxy for signal detection. The obtained detection results are shown in section 5.1.

4.3.2. Location of Seismovolcanic Sources From Low-Rank Interstation Cross-Correlation Matrix

This location method (described in Soubestre et al., 2019) is similar to the 3-D source-scanning algorithm described in the previous part, but here we focus on the dominant wavefield. To do that, we focus on the first eigenvector of the network covariance matrix containing information about the location and the mechanism

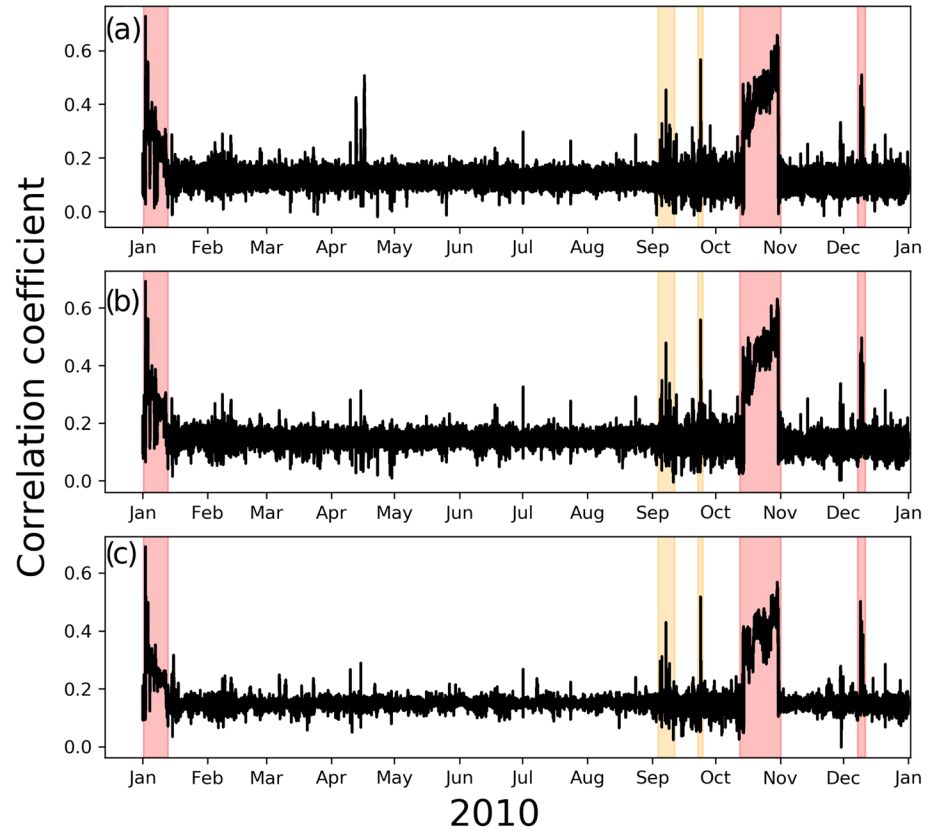


Figure 2. Seismovolcanic activity detection from intercomponent cross correlations at a single station. The three red areas highlight the January, October, and December eruptions, while the two orange areas highlight an increase of seismovolcanic activity at the beginning of September and seismovolcanic activity linked to a dike intrusion on 23 September 2010. (a) Correlation coefficient function $cc_{i,j}^6$ computed for the N-Z component pair of the UV12 seismic station. (b) Average of the three correlation coefficient functions $cc_{i,j}^6$ obtained for the three component pairs of the UV12 seismic station. (c) Average of the averaged function represented in panel (b) on 12 seismic stations whose data availability is stable and identical over 2010 (UV01 to UV14, without UV04 and UV06). High values of this correlation coefficient function are also observed during the seismic crises preceding the three eruptions, and zoomed images are provided in Figures 3a, 4a, and 5a.

of the dominating seismovolcanic tremor source. The first eigenvector represents the most coherent part of the wavefield and acts as a denoising operator. We show in Figure S4 a comparison between the cross-correlation functions (CCFs) from the full recorded seismic wavefield (left panel) and the CCFs extracted from the first eigenvector filtered covariance matrix (right panel). We note that this filtering based on covariance matrix decomposition increases the signal-to-noise ratio, and we therefore use it to improve our location results as it can be seen in Soubestre et al. (2019).

The filtered covariance matrix $\tilde{\mathbf{C}}(f)$ is obtained from the complex outer product of the first eigenvector $v_1(f)$ with himself:

$$\tilde{\mathbf{C}}(f) = v_1(f)v_1^\dagger(f). \quad (6)$$

Then, the time-domain-filtered cross correlations are retrieved by performing the inverse Fourier transform of $\tilde{\mathbf{C}}(f)$ and smoothed to obtain their envelopes, as explained in the previous section.

After the smoothing, each cross-correlation envelope is shifted by the time difference between travel times from every tested point of the 3-D grid to the two considered stations. The network responses are then obtained by stacking the value at zero lag-time of shifted cross-correlation envelopes using Equation 4. In order to better visualize the location result, a normalized network response $\tilde{R}(\mathbf{r})$ is computed:

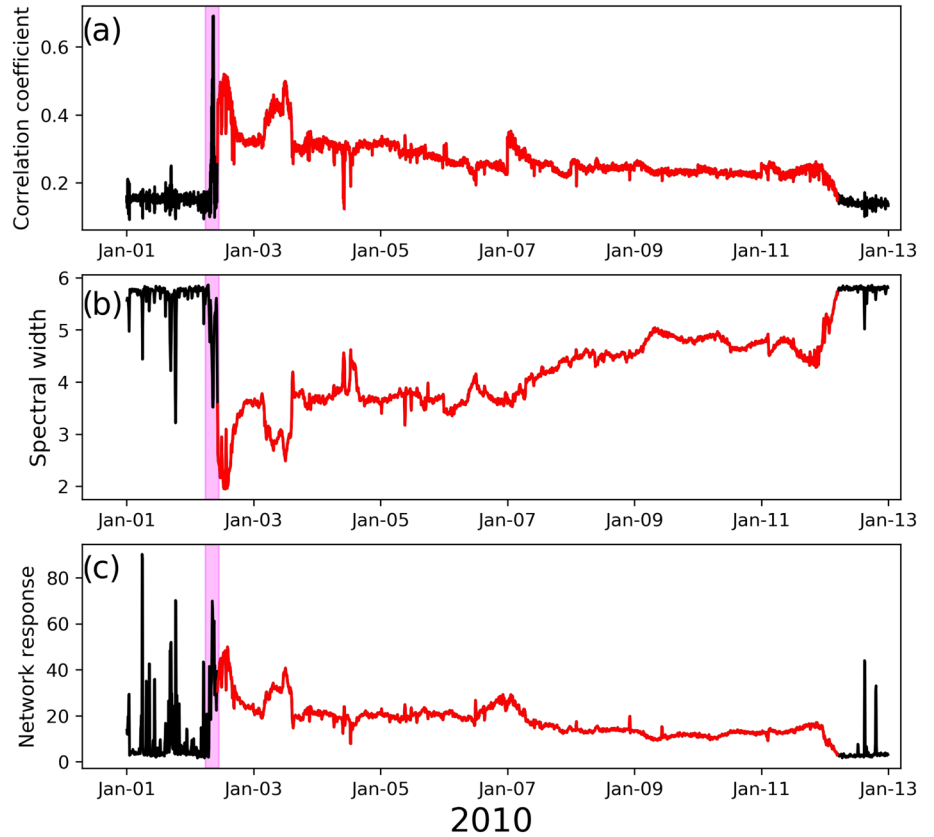


Figure 3. Zoom on the January eruption and its pre-eruptive seismic swarm for (a) the station-averaged $cc_{i,j}^6$ coefficient correlation function, (b) the spectral width, and (c) the NRF. The red color stands for the January seismovolcanic tremor activity, and the fuchsia color stand for the corresponding pre-eruptive seismic crisis, following the color code of Figures 7 and 8.

$$\tilde{R}(\mathbf{r}) = \frac{R(\mathbf{r}) - R^{min}}{R^{max} - R^{min}}, \quad (7)$$

with R^{max} and R^{min} the absolute maximum and minimum of $R(\mathbf{r})$. The obtained location results are shown in section 5.2.

We tested different values of the Gaussian window width used to smooth the cross correlations reconstructed from the first covariance matrix eigenvector. We make our tests on four hours of 15 October 2010 during the October seismovolcanic tremor between 15 and 19 hr, when intercomponent cross correlations remain stable. We thus stack the obtained cross correlations computed in 1,000-s windows during these four hours. We compute their envelopes by testing different values of smoothing Gaussian window width and normalize them by their maxima. We then perform a 3-D backprojection of these obtained cross-correlation envelopes and compute the maximum likelihood value for each tested value of the smoothing Gaussian window width. We show in Figure S5 the maximum likelihood value as a function of the smoothing Gaussian window width. We chose a Gaussian window width value of 1.5 s, corresponding to the corner of the curve in Figure S5 pointed by the red dashed lines, beyond which the maximum likelihood value no longer increases significantly.

5. Results

5.1. Detection of Seismovolcanic Tremors and Other Types of Seismic Activity

Figure 2a shows the result of the $cc_{i,j}^6$ function (described in section 4.1) for the N-Z component pair of station UV12. We note that we can detect the three eruptive seismovolcanic tremors (highlighted in red in the

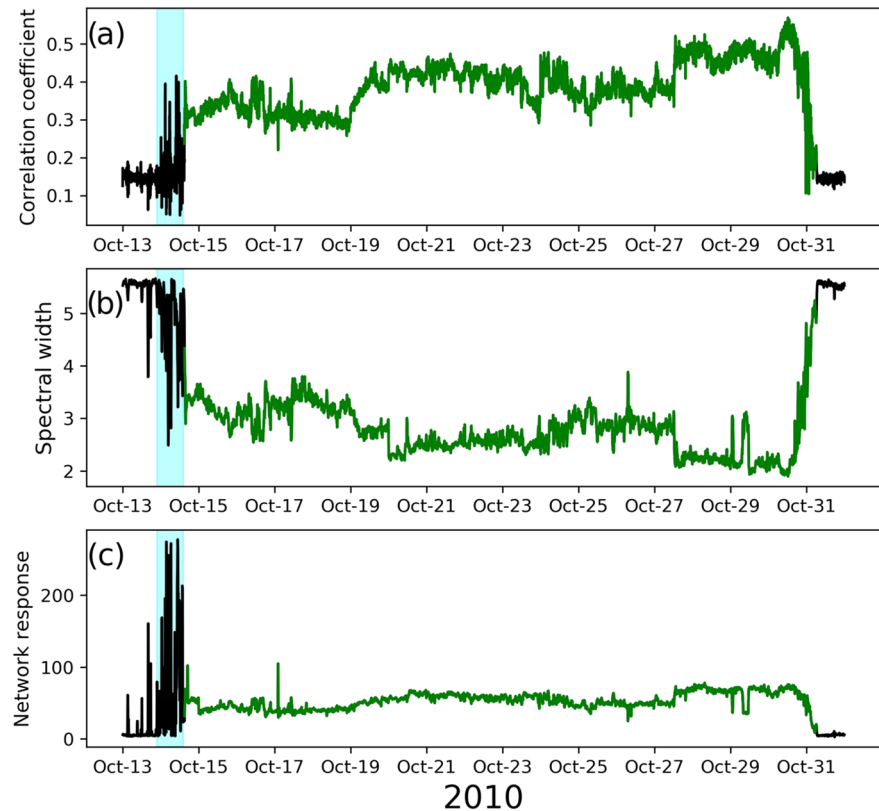


Figure 4. Zoom on the October eruption and its pre-eruptive seismic swarm for (a) the station-averaged $cc_{i,j}^6$ coefficient correlation function, (b) the spectral width, and (c) the NRF. The green color stands for the October seismovolcanic tremor activity, and the cyan color stands for the corresponding pre-eruptive seismic crisis, following the color code of Figures 7 and 8.

figure) only with one component pair of a single station. We can then improve these detection results by averaging the three $cc_{i,j}^6$ functions obtained from the three component pairs, and we show an example for the UV12 station in Figure 2b. In order to improve the signal-to-noise ratio, we perform an average over several stations. We show in Figure 2c the result averaged over 12 stations (36 components) whose continuous records without significant interruption are available through the whole year 2010. We represent some zoom of this station-averaged $cc_{i,j}^6$ function in Figures 3a, 4a, and 5a in which we can observe the high values associated to the seismic crises preceding the three eruptions. In addition to the seismovolcanic tremors and to their preceding seismic swarms, we can also observe high values of the function (highlighted in orange in Figure 2) at the beginning of September when an increase of the seismovolcanic activity is detected and on 23 September 2010 when a dike intrusion occurred without leading to an eruption (Roult et al., 2012).

Figure 6a shows the covariance matrix spectral width (Equation 3) computed on 1,000-s-long overlapping time windows for every frequency; this can be seen as a time-frequency representation of the wavefield recorded by the whole network highlighting the coherent signals. Figure 6b represents the average of this spectral width on the frequency band 1–5 Hz. This function represents another network-based detector, and all three seismovolcanic tremors can be identified with lower values of the spectral width.

Figure 6c shows the NRF (Equation 5) computed every day (time resolution similar to Droznin et al., 2015). This allows us to detect the January and October seismovolcanic tremors (red areas in the figure). However, we cannot detect the December seismovolcanic tremor here because of the temporal resolution. Figure 6d shows the same function computed with a finer time resolution, that is, in 1,000-s-long time windows. We can now detect the three seismovolcanic tremors, and we also observe that the NRF becomes more sensitive to the high-seismicity periods.

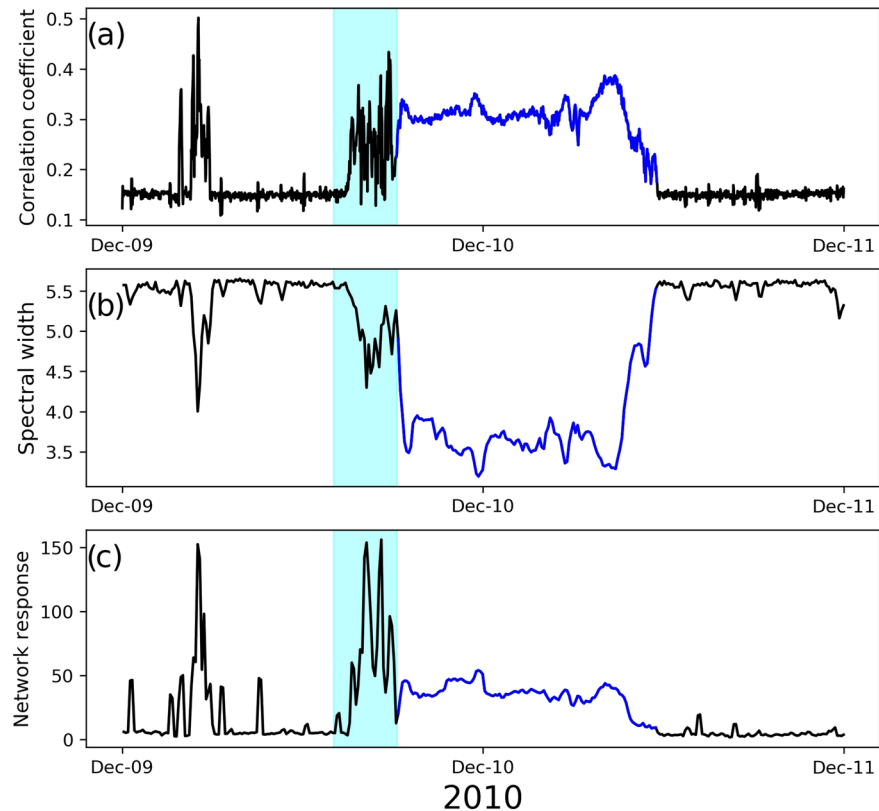


Figure 5. Zoom on the December eruption and its pre-eruptive seismic swarm for (a) the station-averaged $cc_{i,j}^{\phi}$ coefficient correlation function, (b) the spectral width, and (c) the NRF. The blue color stands for the December seismovolcanic tremor activity, and the cyan color stands for the corresponding pre-eruptive seismic crisis, following the color code of Figures 7 and 8.

In addition to the seismovolcanic tremors highlighted in red, we can also detect two other periods of high seismic activity highlighted in orange in the figure: a first one from the beginning of September corresponding to an increase in the seismicity prior to the October eruption and the second one at the end of December, which are followed by an increase of the microseismicity under the summit since the beginning of the year 2011 (OVPF, 2011). The pre-eruptive seismic crises corresponding to each eruption are also well detected (see the zoomed images in Figures 3b, 3c, 4b, 4c, 5b, and 5c).

We note that most of the high values observed in the correlation coefficient function and NRF and low values for the spectral width correspond to known volcanic activities highlighted in red for eruptions or orange for earthquakes and injection. However, the origin of others remains unidentified to date (during April for example), and it can correspond to noise or some previously undetected volcanic activity. While the computation of the NRF requires an a priori medium velocity, there is none for the spectral width calculation. Despite this, the two network-based methods result in a similar first-order information, and we observe an anticorrelation when seismovolcanic tremor sources produce high value of the NRF and low value of $\sigma(f)$. Also, by comparing Figures 2 and 6, we note that while the two network-based detectors catch the same seismovolcanic signals, the correlation coefficient function does not detect the seismicity during September (except at the beginning and during the dike intrusion on 23 September 2010) and at the end of December.

A more detailed comparison of two network-based methods is shown in Figure 7 that represents the average spectral width as a function of the NRF. We can see different trends corresponding to clusters of different seismic events. This allows a clear differentiation of the January and October seismovolcanic tremors represented by red and green colors, respectively, as the January seismovolcanic tremor is characterized by lower values of the network response function (see also Figures 3b, 3c, 4b, and 4c). December seismovolcanic

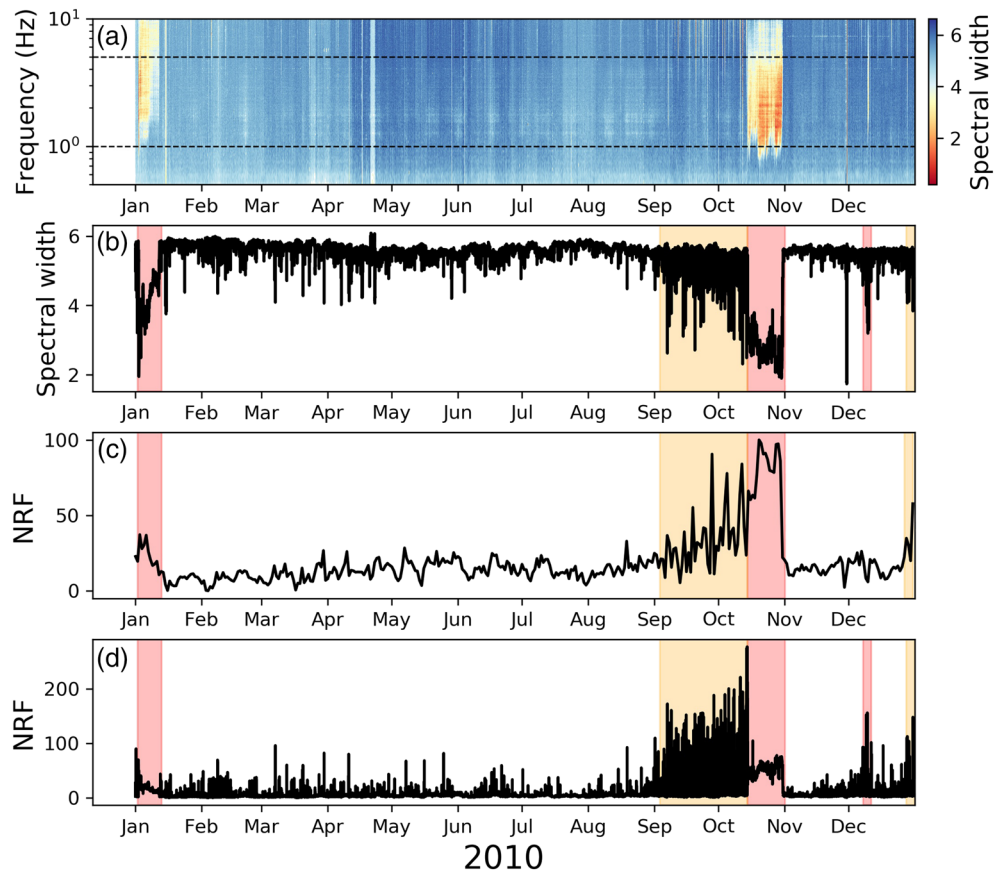


Figure 6. Seismovolcanic activity detection from interstation cross correlations. The red areas highlight periods of detected seismovolcanic tremors, while orange areas highlight periods of high seismic activity in September and at the end of December. (a) Covariance matrix spectral width computed for every frequency on overlapping 1,000-s-long time windows. The two horizontal dashed black lines stand for the lower and upper limits of the covariance matrix spectral width averaging. (b) Average of the covariance matrix spectral width in the frequency band 1–5 Hz. (c) Network response function (Equation 5) computed every day. (d) Network response function computed on 1,000-s-long time windows. In order to limit the impact of the missing stations on the functions (a), (b), and (d), we normalize them by the number of functional stations for each day.

tremor can also be seen in Figure 7 with blue colors, with similar values of the network response function but higher values of the average spectral width than the October seismovolcanic tremor (see also Figures 5b and 5c). We notice that we can thus separate the summit seismovolcanic tremor (which occurred in January) from the two flank seismovolcanic tremors that occurred in the south and northwest flanks in October and December, respectively. We also observe a different temporal evolution for the January and October seismovolcanic tremor. January seismovolcanic tremor is characterized by very low values of spectral width at the beginning of the eruption (very light red in Figure 7), and it evolves until reaching values equivalent to that of seismic noise (dark red in Figure 7). Conversely, the October seismovolcanic tremor begins with intermediate values of spectral width (very light green in Figure 7), then it ends with very low spectral width values (dark green in Figure 7), and, finally, the spectral width becomes higher and higher until the eruption is completely over.

Another trend is distinguishable in Figure 7 with more scattered points represented in purple, which mostly correspond to the earthquakes that occurred during 2010. The September dike intrusion is represented by orange points. Cyan colors correspond to the October and December seismic crises, while the January seismic crisis is represented with fuchsia colors because we see that it is characterized by different values of NRF and spectral width. Gray points in the top left corner of Figure 7, characterized by low values of network response and high values of average spectral width, correspond to seismic noise during the whole year.

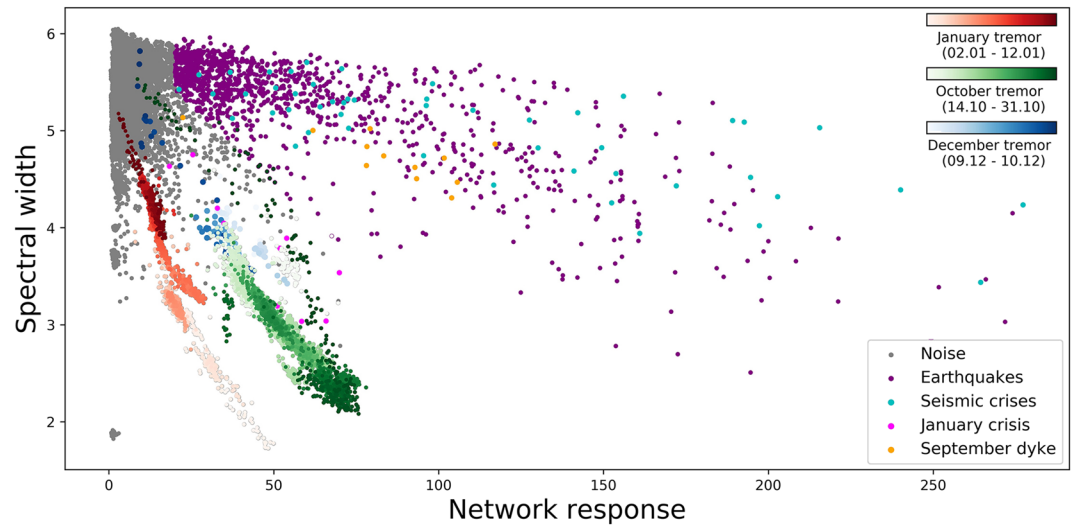


Figure 7. Average spectral width as a function of the network response function. Colors correspond to different clusters of events. The three seismovolcanic tremors are represented with color gradations from lightest to darkest in order to observe their evolution over time. Red colors stand for the January seismovolcanic tremor with corresponding spectral width and network response represented in Figures 3b and 3c, respectively. Green colors stand for the October seismovolcanic tremor as represented in Figures 4b and 4c. Blue colors stand for the December seismovolcanic tremor (see Figures 5b and 5c). Gray points correspond to noise. Purple colors stand for the earthquakes that occurred during 2010. Cyan colors correspond to the October and December seismic crises, while the January seismic crisis is represented with fuchsia colors. The September dike intrusion is represented by orange points.

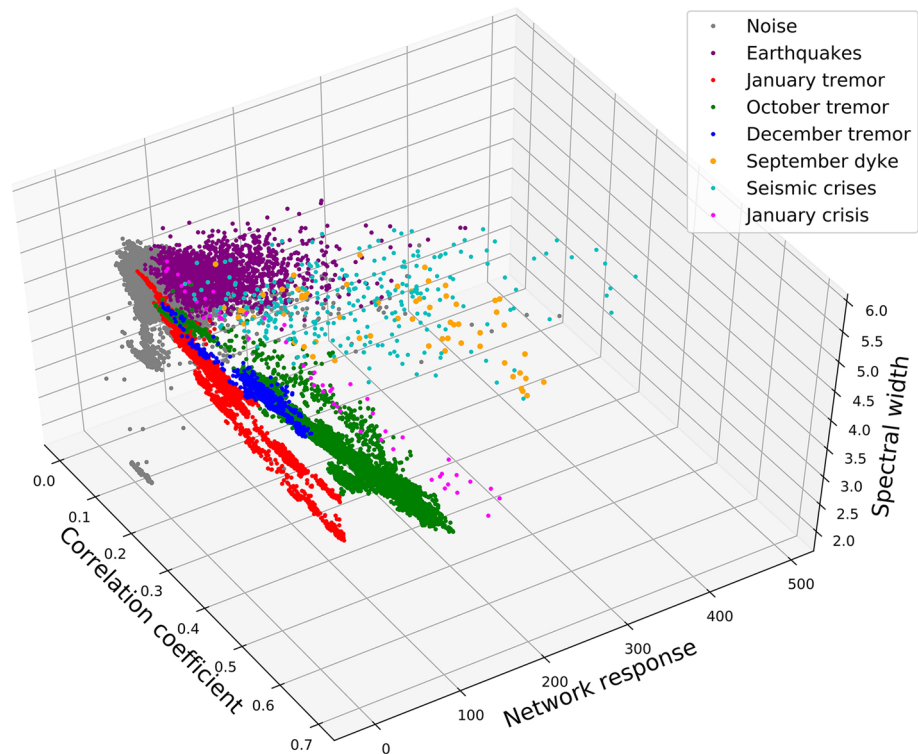


Figure 8. 3-D comparison between the station-averaged $cc_{i,j}^6$ function labeled as “correlation coefficient,” the NRF, and the average spectral width. Gray colors stand for the seismic noise, and purple colors stand for the earthquakes. The January, October, and December seismovolcanic tremors are represented by red, green, and blue colors, respectively. The orange color stands for the dike intrusion that occurred in September, Fuchsia colors stand for the January pre-eruptive seismic crisis, and Cyan colors stand for the October and December pre-eruptive seismic crises.

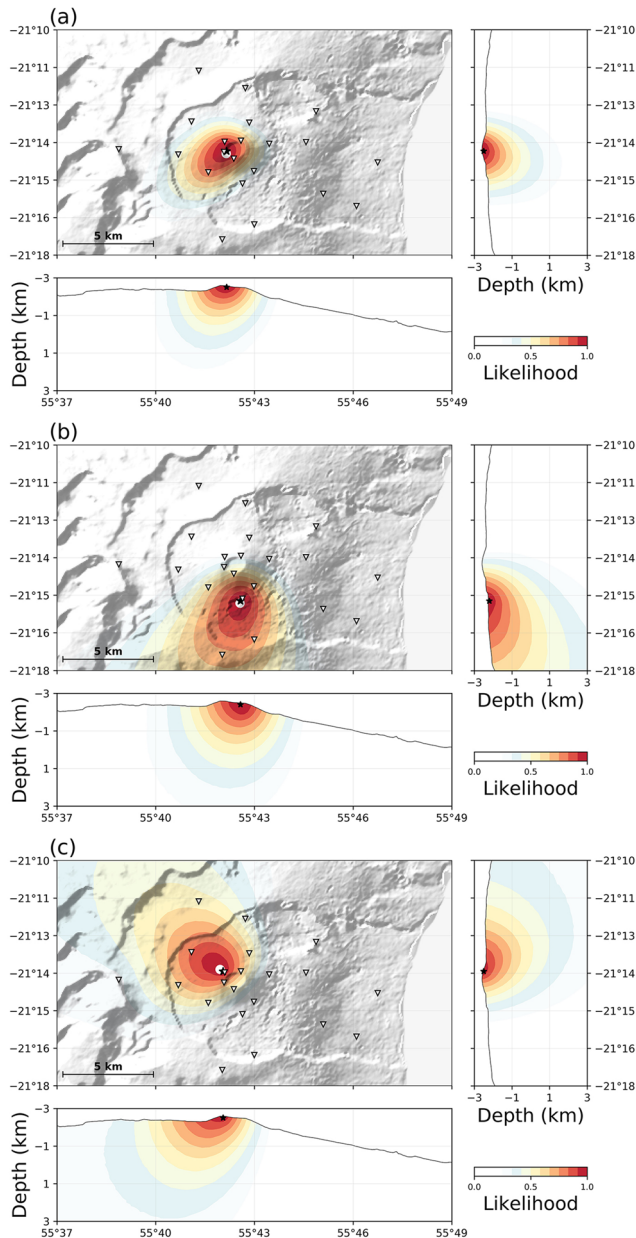


Figure 9. Normalized likelihood functions \bar{R} calculated from the covariance matrix first eigenvectors for (a) 3 January 2010, (b) 15 October 2010, and (c) the 15 hr of the December eruption between 9 and 10 December 2010. The black stars stand for the location of the source with the maximal likelihood value, and the white dot points for the eruptive sites. 3-D location is performed using a 1-D S wave velocity of the PdF volcano from Mordret et al. (2015).

spectral width is computed in 200-s-long overlapping time windows. Figure 10 shows the result of such enhanced seismic event detection and location during the first day of the October eruption (14 October 2010) with pre-eruptive seismic crisis and the seismovolcanic tremor starting at 15:00. We can clearly distinguish discrete VT events that occurred in the seismic crisis in Figure 10a in difference with the continuous following seismovolcanic tremor.

Then we perform a 3-D location by focusing on the first eigenvector of the covariance matrix computed for this day. We stack 10 consecutive 200-s-long overlapping windows, to end up with a location point every

We also note a few points on the bottom left of Figure 7, characterized by very low values of the average spectral width, that correspond to a few hours in the end of November where there was a technical problem and several stations were down.

Finally, we can also make a 3-D comparison between the station-averaged $cc_{i,j}^6$ function (whose zoom during eruptions are shown in Figures 3a, 4a, and 5a), the NRF, and the spectral width as seen in Figure 8. Before comparing all the three functions, we recalculated the NRF and the spectral width with 200-s-long overlapping windows, and we computed a moving average between six consecutive windows. In addition to the separation between summit and flank seismovolcanic tremors, we can also distinguish the intrusion that occurred for a few hours on 23 September 2010 (Roult et al., 2012) represented with orange points. Moreover, we can on the one hand distinguish the pre-eruptive seismic swarms from the others VTs colored in purple and on the other hand distinguish the January seismic swarm colored in fuchsia from the October and December seismic swarms colored in cyan.

5.2. Location of Seismovolcanic Tremor Sources

Figure 9 shows the seismovolcanic tremor sources location results in 3-D based on the extraction of the dominant wavefield (as explained in section 4.3.2, using a Gaussian window width of 1.5 s to smooth the CCFs and a 1-D S wave velocity model from Mordret et al. (2015). We calculate the daily covariance matrix by setting $M=50$ and $\delta t=40$ s to end up with 1,000-s-long windows that overlap with a 50% factor. Figure 9 shows the seismovolcanic tremor sources location results corresponding to the January eruption (Figure 9a), the October eruption (Figure 9b), and the December eruption (Figure 9c). We define a 3-D grid with points spaced every 200 m in order to compute the likelihood function that is then normalized using the Equation 7. For Figures 9a and 9b, we stacked the 1,000-s overlapping windows for 3 January 2010 and 15 October 2010, respectively, while we stacked them only for the 15 hr of eruption between 9 and 10 December 2010 for Figure (9c). We observe that the seismovolcanic tremors seem to be located directly under the eruptive fissure for these three eruptions.

5.3. Pre-eruptive Swarms

To focus on details of VT events that occurred in the observed pre-eruptive seismic swarms, we modify the temporal normalization of the data, and instead of applying the running absolute mean normalization (following Bensen et al., 2007; Seydoux, Shapiro, De Rosny, et al., 2016), we divide the traces (once spectral whitening is applied) by their mean absolute deviation (MAD). We also enhance the temporal resolution of the covariance matrix analysis and modified the parameters introduced in section 4.2 by setting $M=25$ and $\delta t=16$ s. As a result, the covariance matrix

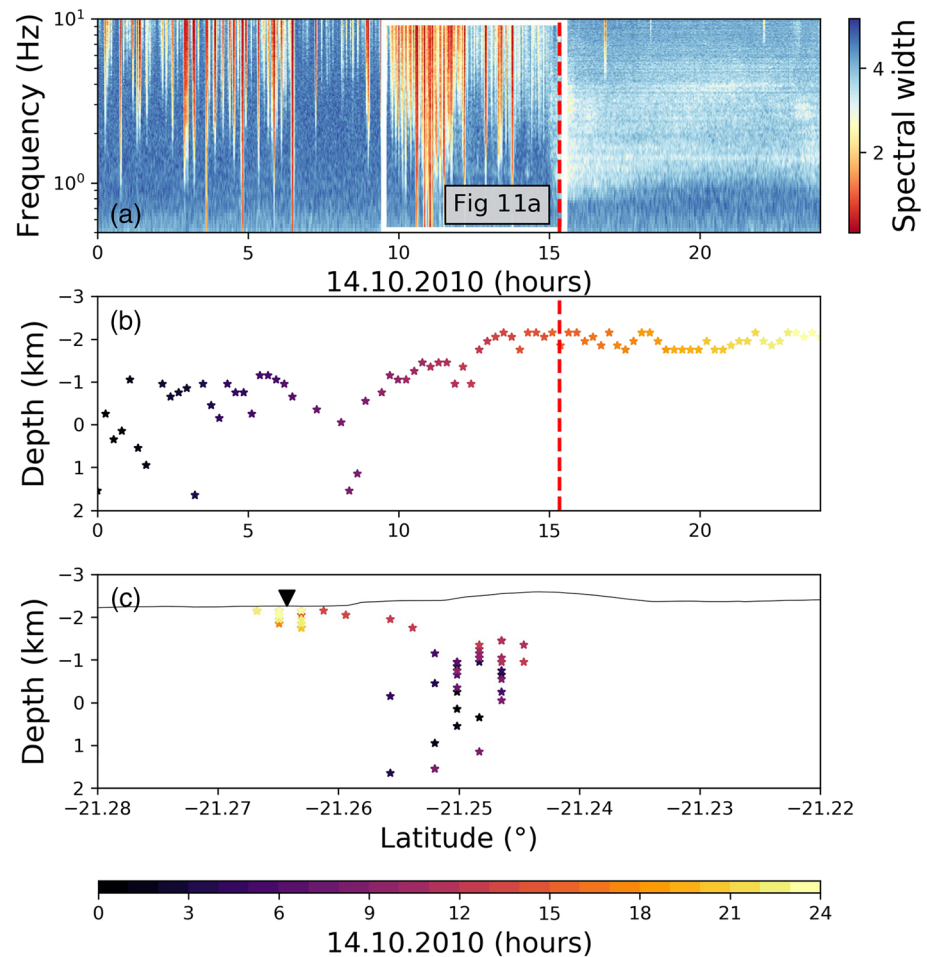


Figure 10. (a) Zoom on the covariance matrix spectral width calculated on 200-s overlapping time windows during 14 October 2010, the first day of the October eruption. Red line stands for the beginning of the eruption. The white frame corresponds to the zoom represented in Figure 11a. (b) 3-D location of the detected seismic signals on 1,000-s time window during 14 October 2010; the depth is represented as a function of time, and the red vertical dashed line stands for the eruption beginning. (c) Same location with the depth as a function of latitude and the colors represent the windows central times. The black triangle at the surface stands for the eruptive site position.

1,000 s. Figure 10b shows the source depth as a function of time, and Figure 10c represents the source depth as a function of the latitude with the symbol colors corresponding to the windows central times.

We observe that VT events that occurred since the beginning of the day and during the seismic crisis are located under the summit dome between ± 1 km around the sea level, which is quite in agreement with what is typically observed for pre-eruptive swarms at PdF. For example, Schmid (2011) located VT events from the 14 October 2010 seismic swarms beneath summit crater between 500 m below sea level and 1,000 m above sea level. Then the seismicity seems to migrate toward the eruption site in the south flank for October eruption. Using template matching and relocation techniques, Duputel et al. (2019) show a clear correlation between pre-eruptive earthquake locations and the azimuth of eruptive sites which is consistent in our case with the presence of VT earthquakes in the southern branch of the summit cone before the migration.

In Figure 11a, a zoom of the spectral width is represented for 14 October 2010 between 09:30 (beginning of the seismic swarm main part) and 15:30 (10 min after the eruption onset). Figure 11b shows an example of a 3-D location on a 200-s-long window of a VT event that occurred at 10:30, situated 1 km above the sea level under the summit cone. In addition to the seismovolcanic tremor and VT events constituting the pre-eruptive seismic swarm, the computation of the covariance matrix spectral width allows also the detection of another type of recently discovered seismic swarm of events characterized by a very high frequency

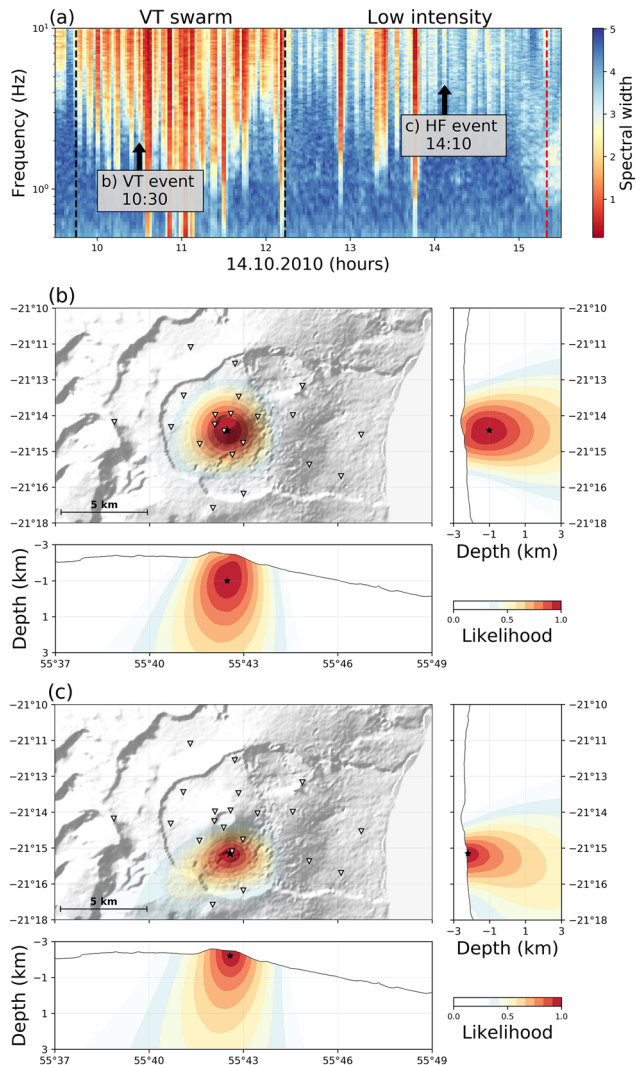


Figure 11. (a) Zoom of the covariance matrix spectral width on 14 October 2010 between the beginning of the seismic swarm main part (09:30) and 10 min after the eruption onset. The two black arrows show the timing of the two events with locations shown in panels (b) and (c). The two vertical dashed black lines stand for the beginning and the end of the VT swarm main part. Then there is a phase of low-intensity seismicity with a small number of VT events. During this phase, the lateral migration of the dike begins, and we can observe a coherent high-frequency swarm. The red vertical dashed line marks the onset of the seismovolcanic tremor and associated eruption. (b) Likelihood functions \hat{R} calculated from the covariance matrix first eigenvectors, 14 October 2010 for a VT event at 10:30 and (c) for an HF event that is part to the high-frequency seismic swarm.

interpreted to be linked to the volcanic edifice deformation induced by magma pressure build-up and injection (Brengruier et al., 2012).

The “single-station intercomponent cross correlations” method can be implemented on volcanoes monitored by a small number of stations. Among the two network-based methods, the “covariance matrix” detector has some advantage because it does not require a priori information about the wave propagation velocity. Additional advantage of network based-methods is their ability to locate seismovolcanic tremor sources. In the case of a network with significant number of well distributed stations, the 3-D location based on “spatially filtered” cross correlations (reconstructed from dominant covariance matrix eigenvector) can be done. Apart from the seismic data quality, the accuracy of such location depends on the knowledge of the internal velocity

content (called HF swarm) (De Barros et al., 2013). As stated by Roult et al. (2012), the classical sequence of events preceding an eruption at PdF is as follows: a first increase of VT events, a swarm of VT with larger magnitudes, then a seismically quiet or low intensity sequence with small number of VT events linked to magma migration, followed by the seismovolcanic tremor onset and the eruptive fissure opening. During the quiescent period between the swarm and the seismovolcanic tremor, De Barros et al. (2013) identified a swarm of HF events on 14 October 2010 since 13:00, located in the area of the eruptive fracture in the south flank and interpreted as a response of the shallow part of the edifice to the stress changes due to the dike propagation. We can observe in Figure 11a some coherent signals between the end of the VT swarm and the seismovolcanic tremor, in particular from 14:00 to 15:00, for frequencies larger than 3 Hz. We represent in Figure 11c an example of a 3-D location on a 200-s-long window of an HF event that occurred at 14:10. There is therefore a migration of the seismicity from the pre-eruptive seismic swarm under the summit cone at the sea level toward an HF swarm superficially near the future eruptive site more than 1 hr before the eruption.

6. Discussion and Conclusions

In this paper, we tested methods that use the phase information contained in continuous seismic signals to study seismovolcanic tremors. First, we introduced a new method of detection of seismovolcanic tremors based on stability of intercomponent cross correlations at a single station. In a next step, we systematically compared this new method with two previously proposed network-based methods by applying all three methods to continuous data recorded by stations of the PdF volcano observatory seismic network during 2010. The second method based on the network covariance matrix has been previously applied to the data set used in this paper by Seydoux, Shapiro, De Rosny, et al. (2016). However, in this previous paper, the time resolution of the analysis was relatively low (1 day), and here we increased it to be able to detect individual volcanic earthquakes. The third method called “network response function” (Droznin et al., 2015) has been applied for the first time to the PdF data and in a 3-D grid considering a 1-D S wave velocity model.

All three methods have been demonstrated to be very sensitive to seismovolcanic tremors and detected all three eruptive seismovolcanic tremors that occurred during 2010. They are also capable of detecting strong pre-eruptive seismic swarms. In addition to this, the two network-based methods detect a large number of volcanic earthquakes and, in particular, the significant increase of seismicity during the month preceding the October 2010 PdF eruption as seen in Figure 6. This seismicity increase is well correlated with the measured decrease of seismic velocity that is

structure of the volcano. In this paper, the tests were limited to location using a 1-D *S* wave velocity model. In principle, wave propagation in 3-D velocity models can be easily incorporated. Permana et al. (2019) used a similar method to locate seismovolcanic tremor using a 1-D *S* wave model as in Soubestre et al. (2019) (except that they do not focus on a dominant seismovolcanic tremor source by filtering by the first eigenvector of the covariance matrix). They simulate seismovolcanic tremor sources by combining multiple VTs and show that they are determined with location errors of approximately 1 km or less.

Moreover, with pushing their time resolution, the discussed method could bring insight on the complexity of the eruption dynamics as shown in Figures 3, 4, and 5. For example, we observe in Figures 3b and 7 that for the January seismovolcanic tremor, the spectral width is very low at the beginning and becomes larger and larger over time until it reaches a value equivalent to that corresponding to seismic noise. Conversely, for the October eruption, we see in Figure 4b a more complicated temporal evolution for the spectral width that could reveal a more complex dynamic. By comparing with Figures 4a and 4c, we observe two main changes occurring at the same time from 19 and 27 October 2010 that are linked with intensification of the seismovolcanic tremor amplitude visible on the RSAM measurement in Figure S1. Thus, such methods can also be useful to monitor the seismovolcanic tremor intensity.

Another interesting perspective is to use the results of the multicomponent analysis as input for algorithms of machine learning (ML) to build advanced approaches for detection and classification of different seismovolcanic signals to be used in monitoring the activity and eruptive behavior of volcanoes. Figures 7 and 8 show that, in the space of parameters determined with the multicomponent methods, different types of seismovolcanic activity are separated and form relatively well-defined clusters. It suggests that ML could be applied with this kind of “features” determined from the data of the PdF seismic network. Previous applications of ML to the PdF seismological data used features derived from individual sensors to study volcanic earthquakes (Hibert et al., 2017; Maggi et al., 2017) and seismovolcanic tremors (Ren et al., 2020). The eventual advantage of multistation features is that they incorporate interlocation phase differences and are, therefore, sensitive to the location and the mechanism of the signal sources.

Data Availability Statement

The data used are publicly available and can be found online. The seismic data used for this study were provided by the Observatoire Volcanologique du Piton de la Fournaise (OVPF). The permanent network data (<https://www.fdsn.org/networks/detail/PF/>) can be downloaded from the IGP Data Center (<http://ws.ippg.fr/fdsnws/dataselect/1/>), the RESIF data center (<http://ws.resif.fr/fdsnws/dataselect/1/>), or the IRIS Data Management Center (IRISDMC, <http://service.iris.edu/fdsnws/dataselect/1/>). The UnderVolc data (<https://doi.org/10.15778/RESIF.YA2009>) are available from the RESIF data center.

Acknowledgments

This study was financially supported by the European Research Council (ERC) under the European Union Horizon 2020 Research and Innovation Programme (Grant Agreement 787399-SEISMAZE) and by the Russian Ministry of Education and Science (Grant No. 14.W03.31.0033) for N. S. We acknowledge support from the European Research Council under the European Union Horizon 2020 Research and Innovation Programme (Grant Agreement 742335, F-IMAGE). Computations were performed using the IGP High-Performance Computing infrastructure S-CAPAD (supported by the Ile-de-France region via the SESAME programme, by France-Grille, and by the CNRS MASTODONS programme). We thank two anonymous reviewers whose comments helped to improve and to clarify the manuscript. This is IGP contribution number 4146.

References

- Bachelery, P. (1981). Le Piton de la Fournaise (Ile de la Réunion): Etude volcanologique, structurale et pétrologique (Thèse de doctorat), Université de Clermont-Ferrand II.
- Ballmer, S., Wolfe, C. J., Okubo, P. G., Haney, M. M., & Thurber, C. H. (2013). Ambient seismic noise interferometry in Hawai'i reveals long-range observability of volcanic tremor. *Geophysical Journal International*, *194*, 512–523.
- Battaglia, J., & Aki, K. (2003). Location of seismic events and eruptive fissures on the Piton de la Fournaise volcano using seismic amplitudes. *Journal of Geophysical Research*, *108*(B8), 2364. <https://doi.org/10.1029/2002JB002193>
- Battaglia, J., Aki, K., & Ferrazzini, V. (2005). Location of tremor sources and estimation of lava output using tremor source amplitude on the Piton de la Fournaise volcano: 1. Location of tremor sources. *Journal of Volcanology and Geothermal Research*, *147*, 268–290.
- Battaglia, J., Brenguier, F., & Roult, G. (2016). Seismic monitoring at Piton de la Fournaise. In P. Bachelery, J.-F. Lénat, A. DiMuro, & L. Michon (Eds.), *Active volcanoes of the south-west Indian Ocean* (pp. 223–242). Berlin, Heidelberg: Springer.
- Bensen, G., Ritzwoller, M., Barmin, M., Levshin, A., Lin, F., Moschetti, M., et al. (2007). Processing seismic ambient noise data to obtain reliable broad-band surface wave dispersion measurements. *Geophysical Journal International*, *169*(3), 1239–1260.
- Bonneville, A. (1990). Structure de la lithosphère. In J.-F. Lénat (Ed.), *Le volcanisme de La Réunion, monographie* (pp. 1–18). Clermont-Ferrand: Observatoire de physique du globe de Clermont: Centre de recherches volcanologiques.
- Brenguier, F. (2014). UnderVolc experiment, 2009–2011, code YA (Understanding volcanic processes). RESIF—Réseau Sismologique et géodésique Français. Terrestrial seismic network. <https://doi.org/10.15778/RESIF.YA2009>
- Brenguier, F., Kowalski, P., Staudacher, T., Ferrazzini, V., Lauret, F., Boissier, P., et al. (2012). First results from the UnderVolc high resolution seismic and GPS network deployed on Piton de la Fournaise volcano. *Seismological Research Letters*, *83*, 97–102.
- Chouet, B. A. (1996). Long-period volcano seismicity: Its source and use in eruption forecasting. *Nature*, *380*, 309–316. <https://doi.org/10.1038/380309a0>
- Chouet, B. A., & Matoza, R. S. (2013). A multi-decadal view of seismic methods for detecting precursors of magma movement and eruption. *Journal of Volcanology and Geothermal Research*, *252*, 108–175.

- Courtilot, V., Besse, J., Vandamme, D., Montigny, R., Jaeger, J., & Cappetta, H. (1986). Deccan flood basalts at the Cretaceous/Tertiary boundary? *Earth and Planetary Science Letters*, *80*, 361–374.
- De Barros, L., Bean, C. J., Zecevic, M., Brenguier, F., & Peltier, A. (2013). Eruptive fracture location forecasts from high-frequency events on Piton de la Fournaise volcano. *Geophysical Research Letters*, *40*, 4599–4603. <https://doi.org/10.1002/grl.50890>
- Droznin, D., Shapiro, N. M., Droznina, S. Y., Senyukov, S., Chebrov, V., & Gordeev, E. (2015). Detecting and locating volcanic tremors on the Klyuchevskoy group of volcanoes (Kamchatka) based on correlations of continuous seismic records. *Geophysical Journal International*, *203*(2), 1001–1010.
- Duputel, Z., Lengline, O., & Ferrazzini, V. (2019). Constraining spatiotemporal characteristics of magma migration at Piton De La Fournaise volcano from pre-eruptive seismicity. *Geophysical Research Letters*, *46*, 119–127. <https://doi.org/10.1029/2018GL080895>
- Endo, E. T., & Murray, T. (1991). Real-time seismic amplitude measurement (RSAM): A volcano monitoring and prediction tool. *Bulletin of Volcanology*, *53*(7), 533–545. <https://doi.org/10.1007/BF00298154>
- Goldstein, P., & Chouet, B. (1994). Array measurements and modeling of sources of shallow volcanic tremor at Kilauea volcano, Hawaii. *Journal of Geophysical Research*, *99*(B2), 2637–2652.
- Haney, M. M. (2014). Backprojection of volcanic tremor. *Geophysical Research Letters*, *41*, 1923–1928. <https://doi.org/10.1002/2013GL058836>
- Hibert, C., Provost, F., Malet, J.-P., Maggi, A., Stumpf, A., & Ferrazzini, V. (2017). Automatic identification of rockfalls and volcano-tectonic earthquakes at the Piton de la Fournaise volcano using a random forest algorithm. *Journal of Volcanology and Geothermal Research*, *340*, 130–142. <https://doi.org/10.1016/j.jvolgeores.2017.04.015>
- Lénat, J.-F., & Bachèlery, P. (1990). Structure et fonctionnement de la zone centrale du Piton de la Fournaise. In J.-F. Lénat (Ed.), *Le volcanisme de La Réunion* (pp. 257–296). Clermont-Ferrand: Observatoire de physique du globe de Clermont: Centre de recherches volcanologiques.
- Maggi, A., Ferrazzini, V., Hibert, C., Beauducel, F., Boissier, P., & Amemoutou, A. (2017). Implementation of a multistation approach for automated event classification at Piton de la Fournaise volcano. *Seismological Research Letters*, *88*(3), 878–891.
- McNutt, S. R., & Nishimura, T. (2008). Volcanic tremor during eruptions: Temporal characteristics, scaling and constraints on conduit size and processes. *Journal of Volcanology and Geothermal Research*, *178*(1), 10–18.
- McNutt, S. R., & Roman, D. C. (2015). Chapter 59—Volcanic seismicity, (2nd ed.). In H. Sigurdsson (Ed.), *The encyclopedia of volcanoes (second edition)* (pp. 1011–1034). Amsterdam: Academic Press.
- Métaxian, J.-P., Lesage, P., & Valette, B. (2002). Locating sources of volcanic tremor and emergent events by seismic triangulation: Application to Arenal volcano, Costa Rica. *Journal of Geophysical Research*, *107*(B10), 2243.
- Mordret, A., Rivet, D., Landés, M., & Shapiro, N. M. (2015). Three-dimensional shear velocity anisotropic model of Piton de la Fournaise volcano (La Réunion Island) from ambient seismic noise. *Journal of Geophysical Research: Solid Earth*, *120*, 406–427. <https://doi.org/10.1002/2014JB011654>
- OVPF (2011). Activity bulletin 08/01/2011, ISSN 2610-5101.
- Peltier, A., Famin, V., Bachèlery, P., Cayol, V., Fukushima, Y., & Staudacher, T. (2008). Cyclic magma storages and transfers at Piton de La Fournaise volcano (La Réunion hotspot) inferred from deformation and geochemical data. *Earth and Planetary Science Letters*, *270*, 180–188. <https://doi.org/10.1016/j.epsl.2008.02.042>
- Permana, T., Nishimura, T., Nakahara, H., Fujita, E., & Ueda, H. (2019). Reliability evaluation of volcanic tremor source location determination using cross-correlation functions. *Geophysical Journal International*, *220*(2), 1300–1315. <https://doi.org/10.1093/gji/ggz523>
- Ren, C. X., Peltier, A., Ferrazzini, V., Rouet-Leduc, B., Johnson, P. A., & Brenguier, F. (2020). Machine learning reveals the seismic signature of eruptive behavior at Piton de la Fournaise Volcano. *Geophysical Research Letters*, *47*, e2019GL085523. <https://doi.org/10.1029/2019GL085523>
- Roman, D. C., & Cashman, K. V. (2006). The origin of volcano-tectonic earthquake swarms. *Geology*, *34*(6), 457–460. <https://doi.org/10.1130/G22269.1>
- Rost, S., & Thomas, C. (2002). Array seismology: Methods and applications. *Reviews of Geophysics*, *40*(3), 2–1–2–27. <https://doi.org/10.1029/2000RG000100>
- Roult, G., Peltier, A., Taisne, B., Staudacher, T., Ferrazzini, V., & Di Muro, A. (2012). A new comprehensive classification of the Piton de la Fournaise activity spanning the 1985–2010 period. Search and analysis of short-term precursors from a broad-band seismological station. *Journal of Volcanology and Geothermal Research*, *241*, 78–104.
- Schmid, A. (2011). Quelle prédictibilité pour les éruptions volcaniques ? de l'échelle mondiale au piton de la fournaise (Thèse de doctorat), Université de Grenoble.
- Seydoux, L., de Rosny, J., & Shapiro, N. M. (2017). Pre-processing ambient noise cross-correlations with equalizing the covariance matrix eigenspectrum. *Geophysical Journal International*, *210*(3), 1432–1449. <https://doi.org/10.1093/gji/ggx250>
- Seydoux, L., Shapiro, N. M., De Rosny, J., Brenguier, F., & Landes, M. (2016). Detecting seismic activity with a covariance matrix analysis of data recorded on seismic arrays. *Geophysical Journal International*, *204*(3), 1430–1442.
- Seydoux, L., Shapiro, N. M., de Rosny, J., & Landes, M. (2016). Spatial coherence of the seismic wavefield continuously recorded by the USArray. *Geophysical Research Letters*, *43*, 9644–9652. <https://doi.org/10.1002/2016GL070320>
- Shapiro, N. M., & Campillo, M. (2004). Emergence of broadband Rayleigh waves from correlations of the ambient seismic noise. *Geophysical Research Letters*, *31*, L07614. <https://doi.org/10.1029/2004GL019491>
- Shapiro, N. M., Campillo, M., Stehly, L., & Ritzwoller, M. H. (2005). High-resolution surface-wave tomography from ambient seismic noise. *Science*, *307*(5715), 1615–1618. <https://doi.org/10.1126/science.1108339>
- Shapiro, N. M., Ritzwoller, M. H., & Bensen, G. D. (2006). Source location of the 26 sec microseism from cross-correlations of ambient seismic noise. *Geophysical Research Letters*, *33*, L18310. <https://doi.org/10.1029/2006GL027010>
- Soubestre, J., Seydoux, L., Shapiro, N. M., de Rosny, J., Droznin, D. V., Droznina, S. Y., et al. (2019). Depth migration of seismovolcanic tremor sources below the Klyuchevskoy volcanic group (Kamchatka) determined from a network-based analysis. *Geophysical Research Letters*, *46*, 8018–8030. <https://doi.org/10.1029/2019GL083465>
- Soubestre, J., Shapiro, N. M., Seydoux, L., de Rosny, J., Droznin, D. V., Droznina, S. Y., et al. (2018). Network-based detection and classification of seismovolcanic tremors: Example from the Klyuchevskoy volcanic group in Kamchatka. *Journal of Geophysical Research: Solid Earth*, *123*, 564–582. <https://doi.org/10.1002/2017JB014726>
- Staudacher, T., Peltier, A., Ferrazzini, V., DiMuro, A., Boissier, P., Catherine, P., et al. (2016). Fifteen years of intense eruptive activity (1998–2013) at Piton de la Fournaise volcano: A review. In P. Bachèlery, J.-F. Lénat, A. DiMuro, & L. Michon (Eds.), *Active volcanoes of the south-west Indian Ocean* (pp. 139–170). Berlin, Heidelberg: Springer.

- Taisne, B., Brenguier, F., Shapiro, N. M., & Ferrazzini, V. (2011). Imaging the dynamics of magma propagation using radiated seismic intensity. *Geophysical Research Letters*, *38*, 2–6. <https://doi.org/10.1029/2010GL046068>
- Tsekhmistrenko, M., Sigloch, K., & Hosseini, K. (2018). Whole-mantle structure under the Reunion hotspot in the western Indian Ocean from multifrequency P-wave tomography. *EGU General Assembly Conference Abstracts* (pp. 1076). Göttingen: Copernicus Publications.
- Unglert, K., & Jellinek, A. M. (2015). Volcanic tremor and frequency gliding during dike intrusions at Kilauea—A tale of three eruptions. *Journal of Geophysical Research: Solid Earth*, *120*, 1142–1158. <https://doi.org/10.1002/2014JB011596>
- Unglert, K., Radić, V., & Jellinek, A. M. (2016). Principal component analysis vs. self-organizing maps combined with hierarchical clustering for pattern recognition in volcano seismic spectra. *Journal of Volcanology and Geothermal Research*, *320*, 58–74.